The doping of coal-based activated carbon with both B and N for use as the cathode of high performance aqueous zinc-ion hybrid capacitors

Liu Shuyuan[1,2], Tian Zhen[1,2,*], Wang Yanzhong[1,2], Zhou Rui[1,2], Zheng Zhichao[1,2]

(1. *School of Materials Science and Engineering, North University of China, Taiyuan* 030051, *China*;
2. *Shanxi Key Laboratory of Efficient Hydrogen Storage & Production Technology and Application, North University of China, Taiyuan* 030051, *China*)

Abstract: Aqueous zinc-ion capacitors (ZICs) have significant potential as energy storage systems because of their high specific capacity and superior reliability. Heteroatom-doped carbon materials were known to substantially increase the capacitance of ZICs, however the mechanism remains poorly understood. Coal-based activated carbon was functionalized with B and N to serve as the cathode material in ZICs. This modification gave the material a high specific capacity of 371.4 mAh g^{-1} at 1 A g^{-1} and it retained 74% of its initial capacity after 10 000 cycles. Experimental results and density functional theory calculations revealed that pyridinic N plays a crucial role in increasing Zn^{2+} storage, demonstrating superior electrochemical reversibility. This work gives valuable insight into the design of high-capacity and ultrafast pseudocapacitive carbon cathodes for ZICs.

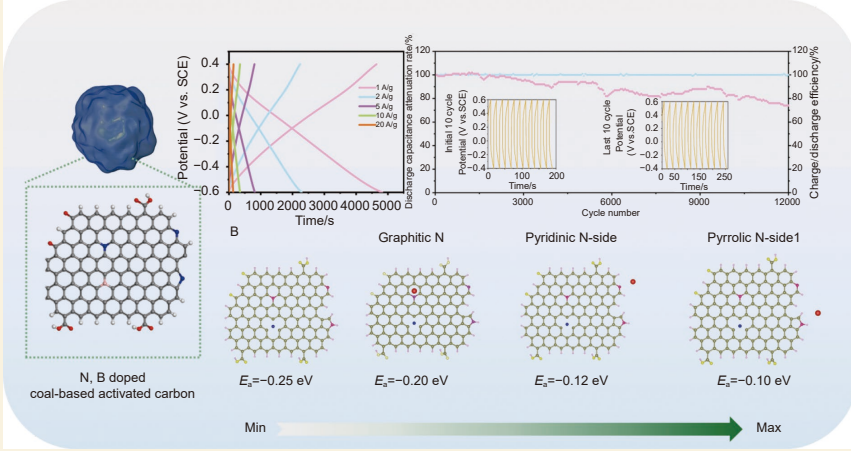

Key words: Heteroatom doping; Zinc-ion capacitor; Coal based activated carbon; Cathode

1 Introduction

The development of sustainable, high-performance energy storage systems is important to address the uneven production and geographic distribution of primary energy sources such as solar and wind energy[1]. To address this challenge, hybrid capacitors have been developed as an advanced electrochemical energy storage system, offering high-rate capability, enhanced energy density, superior power output, and excellent cycling stability. In 2005, Fuji Heavy Industries introduced the concept of the "lithium-ion capacitors (LICs)" with the aim of achieving a synergistic effect that exceeds the sum of its individual components. The LICs consist of a prelithiated graphite anode and an activated carbon cathode[2–4]. However, the shortage of lithium metal and its flammability predicted serious economic risks and environmental problems in the long run. Consequently, researchers began exploring multivalent metal-ion hybrid capacitors based on alternative metals as a viable substitute for LICs. These alternatives include monovalent metals (e.g. Na^+, K^+) and multivalent metals (e.g. Mg^{2+}, Zn^{2+}, Ca^{2+}, Al^{3+}), which are abundant in the Earth's crust and offer higher electron transfer per mole of ions. However, devices based on Mg^{2+}, Ca^{2+} and Al^{3+} usually show poor electrochemical performance in aqueous electrolytes by generating electro-

Received: September 15, 2025
Revised: December 18, 2025
Accepted: December 18, 2025

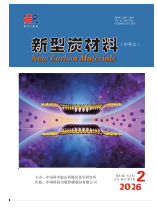

chemically inert by-products passivated at the electrode surface. In contrast, zinc-ion capacitors (ZICs) have excellent reversibility, high stability[5] and high theoretical specific capacity (823 mAh g^{-1})[6–7]. Meanwhile, the low redox potential of Zn/Zn^{2+} extends the operating voltage window of the capacitor, thereby increasing energy and power density[8–9]. However, the ZICs still suffer from unsatisfactory charge storage capability and durability due to the sluggish ion-migration kinetics in carbon cathodes. Thus, the design of highly electroactive and robust carbon nanostructures is crucial for achieving superior electrochemical performance in ZICs.

Carbon-based materials have been extensively studied and utilized as cathodes for ZICs owing to numerous advantages that include low cost, environmental friendliness, and tunable structure. Among these materials, coal-based activated carbon (CAC) has garnered significant attention due to its cost-effectiveness and abundant availability. As a carbonaceous material, CAC possesses a wealth of surface functional groups, making it an excellent raw material for high-quality activated carbon[10–12]. However, CAC exhibits uneven pore distribution and few surface-active sites, which are crucial disadvantages. Excessive micropores make it difficult for electrolyte ions to enter the pores and hinder the transport of ions[13]. The low efficiency of ion adsorption and desorption due to the lack of active sites on the surface of CAC leads to the deterioration of the electrochemical performance of CAC and affect the secondary utilization in the direction of energy storage electrode materials.

As for ZIC cathode materials, there are still significant challenges in developing advanced CAC with abundant active sites, high active site utilization, and rapid kinetics. In this regard, the pore structure and surface chemical state are 2 critical factors influencing the performance of ZICs. The optimal pore size should be tailored to match the dimensions of zinc ions, thereby enriching the ion storage space and enhancing reaction points during rapid adsorption and desorption processes. Additionally, the electrochemical performance of ZICs is significantly influenced by the surface chemical state. Therefore, modifying the surface of carbon materials can effectively promote zinc ion adsorption. For instance, introducing heteroatoms, such as nitrogen (N), boron (B), phosphorous (P) and sulfur (S), particularly N atoms, into the carbon network can effectively modify surface polarization, enhancing wettability towards polar electrolyte ions. This not only facilitates fast ion transfer and provides a large accessible interface for charge storage but also creates additional active sites for pseudocapacitance. Moreover, different types of N doping have distinct effects on electrochemical properties. Pyrrolic N and pyridine N can increase specific capacitance due to their pseudocapacitive contributions, while graphitic N tends to enhance the conductivity of carbon materials[14–16]. Boron, with 3 valence electrons, can function as an electron acceptor. Previous studies have demonstrated that carbon materials modified with N or B atoms exhibit significantly enhanced zinc ion adsorption capabilities[17–20]. However, the effects of various N doping configurations on the charge storage behavior of CAC, including their contributions to electrochemical kinetics and the underlying charge storage mechanisms, remain insufficiently explored. Therefore, elucidating the reaction mechanisms between dopants and the porous structure of CAC is highly desirable. B and N co-doping is employed as a strategic approach to enhance the performance of coal-based activated carbon, and the influence of this co-doping strategy on zinc ion adsorption energy is systematically investigated using density functional theory (DFT).

In this study, ammonium pentaborate tetrahydrate $NH_4B_5O_8{\cdot}4H_2O$ was selected as the B and N precursor owing to its high water solubility and the molecular-level homogeneity of B and N elements, which facilitates more uniform doping of CAC during the hydrothermal process. Consequently, the optimized N, B doped-CAC sample exhibits a large specific surface area with a highly interconnected pore structure, providing additional electro-active sites for efficient electrolytic ion adsorption/desorption and facilitating

ion transport pathways through rapid ion transfer kinetics. DFT calculations demonstrate that N and B co-doping significantly enhance the adsorption capacity for zinc ions and improves electron transfer behavior. This approach offers a promising strategy for the design of ZICs cathodes with high capacity and long-term stability.

2 Experimental

2.1 Materials

Coal-based activated carbon (CAC) was purchased from Foshan Porous Carbon Technology Co., Ltd. $NH_4B_5O_8·4H_2O$ was purchased from Shanghai Macklin Biochemical Technology Co., Ltd. Carboxymethylcellulose sodium (CMC2200) was obtained from Guangdong Canrd New Energy Technology Co.,Ltd. Ketjenblack EC600JD was purchased from Suzhou Sinero Technology Co., Ltd. All chemicals were utilized directly without further purification.

2.2 Preparation of N, B dual-doped coal-based activated carbon

CAC was modified using a facile hydrothermal method. Firstly, 100 mg of CAC was dissolved in 40 mL of deionized water and stirred magnetically for 30 min. Then, 100 mg of $NH_4B_5O_8·4H_2O$ was added to the solution and stirred for another 30 min. The mixed solution was placed in a reactor and reacted at 120, 150 and 180 °C for 6 h, respectively. After centrifuging, cleaning with deionized water, and drying at 80 °C for 24 h, the powdered product of CAC with nanospheres structure was obtained. The sample without $NH_4B_5O_8·4H_2O$ was named CAC, and the other products were named CAC-120, CAC-150 and CAC-180 after reaction at 120, 150 and 180 °C, respectively.

2.3 Materials characterization

The microstructure and morphology of as-prepared samples were characterized by scanning electron microscope (SEM, TESCAN MIRA LMS). The crystal structure of as-prepared samples was analyzed by the Rigaku Miniflex 600 X-ray diffractometer (XRD) with Cu *K*α radiation. Raman spectrum was collected from the HORIBA LabRAM HR Evolution. The X-ray photoelectron spectroscopy (XPS) analysis was performed on a Thermo Scientific ESCALAB model 250Xi using Al *K*α radiation to ascertain the surface elemental composition. The pore structure characteristics at 77 K were detected by N_2 adsorption-desorption instrument (ASAP2020).

2.4 Electrochemical measurements

To prepare the working electrode, active material (80%, wt%), conductive acetylene black (10%, wt%) and CMC (10%, wt%) were mixed in deionized solution and dried to form a uniform paste. After being cast onto a substrate and pressed onto a carbon cloth, the working electrode was prepared with an active material mass loading of approximately 1.0 mg cm^{-2}. In a three-electrode test, a Pt plate and a saturated calomel electrode served as a counter and reference electrode, respectively. At room temperature, the electrochemical performance was tested on the electrochemical workstation (CHI660E), including cyclic voltammetry (CV), constant current charge-discharge (GCD) and electrochemical impedance spectroscopy (EIS). CV and GCD were collected in a wide voltage range of −0.6 to 0.4 V, and EIS was measured in a frequency range of 1×10^{-2} to 1×10^{5} Hz. To further investigate the Zn^{2+} storage performance of as-prepared samples, Swagelok cell was assembled by using 1 mg of the prepared electrode material as the cathode, 8.9 mg CAC as the anode, with the mass being given by Eq. (1)[21], Whatman filter paper as separator and 2 mol L^{-1} $ZnSO_4$ as electrolyte. At room temperature, the electrochemical performance was tested on CHI660E, including CV, GCD and EIS. CV and GCD were collected in a wide voltage range of 0 to 2 V, and EIS was measured in a frequency range of 1×10^{-2} to 1×10^{5} Hz. In addition, the specific capacity (*C*, mAh g^{-1}), energy density (*E*, Wh kg^{-1}) and power density (*P*, W kg^{-1}) were determined by the following Eq. (2-4)[22]:

$$\frac{m^+}{m^-}=\frac{(C_m^-\times\Delta E^-)}{(C_m^+\times\Delta E^+)} \quad (1)$$

$$C=\frac{I\Delta t}{3.6} \quad (2)$$

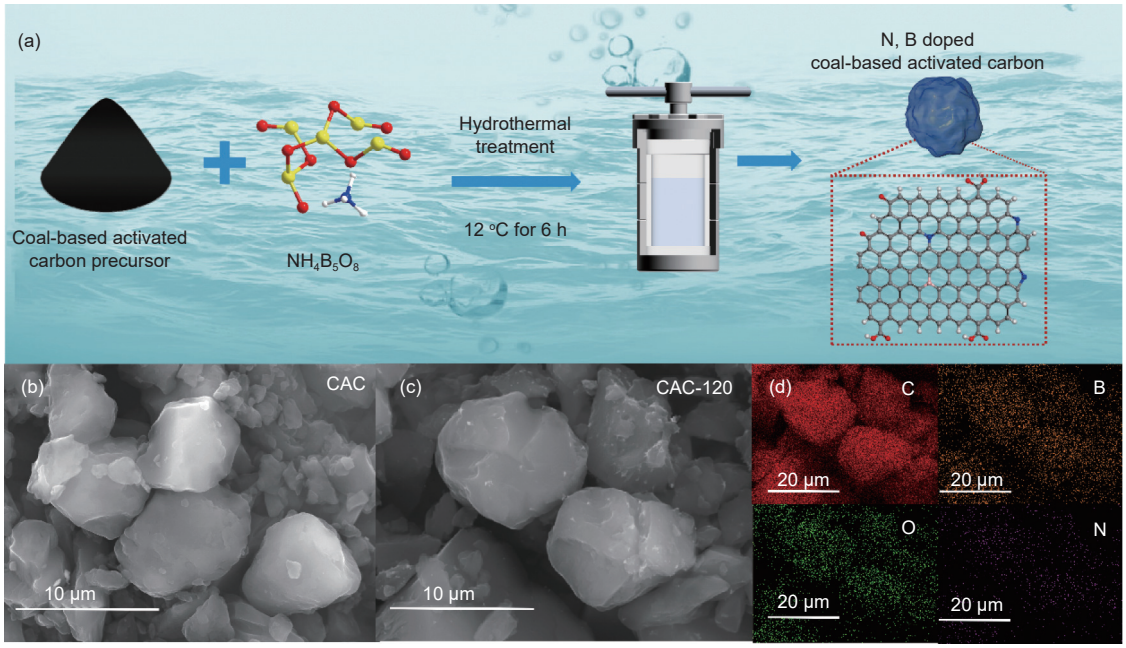

Fig. 1 (a) Schematic illustration of the synthesis process of CAC-120. SEM images of (b) CAC, (c) CAC-120. (d) Elemental mapping images of CAC-120

$$E = \frac{\int VI\mathrm{d}t}{3.6m} \quad (3)$$

$$P = \frac{3600E}{\Delta t} \quad (4)$$

3 Results and discussion

The schematic for preparation of CAC-120 is shown in Fig. 1a, in which the sample was synthesized by a facile hydrothermal method using CAC and $NH_4B_5O_8{\cdot}4H_2O$ as raw materials. The morphology of the prepared samples was observed by SEM technology. Fig. 1b and 1c exhibit the SEM images of CAC and CAC-120, respectively, showing similar porous structures. The SEM image of CAC-120 confirmed the negligible effect on morphologies after the introduction of N and B atoms into the activated carbon matrix. The porous structure remains essentially unchanged with increasing temperature (Fig. S1-S4). The porous structure could facilitate electrolyte ion transport for rapid transport kinetics[23]. The EDS mapping of CAC-120 (Fig. 1d) displays the presence of C, O, N and B elements, indicating a uniform distribution within the carbon matrix. Table S1 was calculated by ICP and organic elements analysis. As shown in the table, the O content is 8.0% (atom fraction), B accounts for 1.8%, and N for 0.8%.

The structures of CAC, CAC-120, CAC-150 and CAC-180 were studied by XRD and Raman spectroscopy. According to Fig. 2a, all samples have 2 broad characteristic peaks at 2θ=24° and 43°, which can be attributed to the graphitic (002) and (100) planes of carbon, respectively. Interestingly, the characteristic peak intensity decreased with decreasing reaction temperature, indicating the amorphous nature of CAC-120, which is favorable for rapid ion transport. As shown in Fig. S5, the XRD pattern of CAC subjected to hydrothermal treatment exhibits a shift toward lower angles and a reduced half-peak width, indicating that the treatment enhances the degree of graphitization. Fig. 2b shows the Raman spectra of CAC, CAC-120, CAC-150 and CAC-180. These 4 samples show 2 main bands at 1358 cm^{-1} (*D* band) and 1600 cm^{-1} (*G* band), which correspond to amorphous sp^3 structure and crystalline sp^2 carbon structure respectively[24–25]. The presence of the *D* band suggests that it originates from an amorphous carbonaceous material and indicates defects or disorder within this material. The I_D/I_G ratio can quantify the extent of imperfections and graphitization[26]. The ratio I_D/I_G increased from 0.847 in CAC to 0.851 in CAC-120, indicating a lower crystallinity of CAC-120, in accord with the XRD results. Furthermore, the *D* band was decomposed into 3 distinct sub-bands using Gaussian-Lorentzian numerical simulations to further investig-

ate the types of defects in the obtained samples. As shown in Fig. 2c, the D band (~ 1340 cm^{-1}) of the CAC-120 sample can be attributed to the structural defects in the armchair configuration. The D_2 band is located at about 1500 cm^{-1}, which is related to the defects caused by organic molecules or functional groups in the carbon structure[27]. The T band observed at about 1200 cm^{-1} corresponds to the alternation between sp^2 and sp^3 bonding configurations, which is related to ionic impurities[28]. The I_D/I_G value increases from 0.842 of CAC (Fig. 2d) to 0.847 of CAC-120 (Fig. 2c), further confirming the low crystallinity of CAC-120. The intensity peak ratio of I_T/I_G is a key factor for predicting the presence of doped elements in the carbon structure. The calculated I_T/I_G value of CAC-120 (Fig. 2c) (0.93) was higher than that of CAC (Fig. 2d) (0.92), indicating that nitrogen and boron were successfully doped into the carbon structure, which is favorable for providing additional active sites for Zn^{2+} storage. The pore structure of electrode materials plays a crucial role in influencing the electrochemical performance of energy storage devices. Nitrogen adsorption-desorption measurements were conducted to characterize the porous properties of the samples. The N_2 adsorption-desorption isotherms are shown in Fig. 2e, in which both samples exhibit typical Type I isotherms. The sudden increase of adsorption at low relative pressure (p/p_0 < 0.01) indicates that there are abundant micropores in CAC and CAC-120 samples[29]. The hysteresis loop observed in the high relative pressure range (0.5-0.9) suggests the presence of mesopores. Additionally, a slight increase in adsorption when the relative pressure exceeds 0.9 indicates the presence of some macropores. The BET analysis of CAC-120 exhibits a higher nitrogen adsorption capacity compared to the undoped samples (Fig. S6). Furthermore, the pore size distributions (Fig. S7) show that CAC and CAC-120 have narrow pore sizes of 2.56 and 2.53 nm, respectively, which are considered beneficial for the charge storage process[30]. Employing the Brunauer-Emmett-Teller (BET) method, the specific surface areas of CAC and CAC-120 were calculated to be 1784 and 1925 $m^2\ g^{-1}$, respectively, suggesting that CAC-120 can provide a large number of electroactive sites available to enhance ion adsorption and desorption. More detailed information about pore structure properties of CAC and CAC-120 is listed in Fig.2f and Table S2. The total pore volumes (V_t) of the 2 samples increased from 0.80 to 0.83 $cm^3\ g^{-1}$, which demonstrates that the heteroatoms have a positive impact on controlling the porosity. Furthermore, the pro-

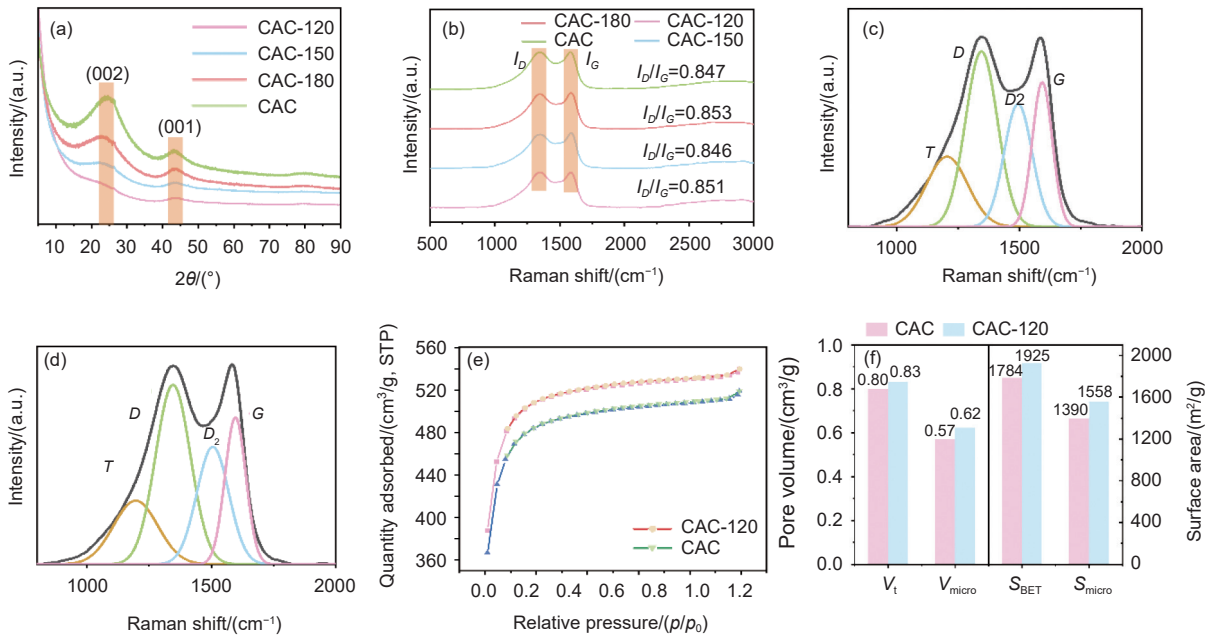

Fig. 2 (a) XRD patterns. (b) Raman spectra. Deconvoluted Raman spectra of (c) CAC-120 and (d) CAC. (e) N_2 adsorption-desorption isotherms of CAC and CAC-120. (f) Pore volumes and specific surface areas of CAC and CAC-120

portions of micropore volume to total pore volume (V_{mic}/V_{total}) for CAC and CAC-120 were calculated to be 0.71 and 0.75, respectively. This result may be due to the decomposition of ammonium pentaborate, which generates a large amount of gas, contributing to the formation of micropores, which is beneficial for enhanced ion transport[31−32]. Co-doping of N and B is also beneficial to the penetration and wetting of electrolyte into CAC-120 cathode, which is confirmed by the decrease of contact angle between aqueous electrolyte and electrode from 139° of CAC and 130° of CAC-120 (Fig. S8).

X-ray photoelectron spectroscopy (XPS) analysis was conducted to determine the heteroatom doping, chemical states, surface composition, and carbon structural reorganization in the samples. As depicted in Fig. S9, the full XPS spectra of CAC-120 exhibit 4 peaks at 284.01, 531.76, 399.22 and 191.23 eV, indicating the presence of C 1s, O 1s, N 1s and B 1s in the carbon matrix. The high-resolution XPS spectra of C 1s, O 1s, N 1s and B 1s in CAC and CAC-120 are shown in Fig. 3. As shown in Fig. 3a, the C 1s signal of CAC-120 can be fitted into 4 peaks at 283.8, 284.8, 287.2 and 289 eV, which are corresponding to the C−C/C=C, C−N/C−B, C−O/C=O and −COOH groups, respectively. As can be seen in Fig. 3a, the C−N/C−B content in CAC-120 is higher than that in CAC, whereas the C−O/C=O content is lower. This discrepancy can be attributed to the slightly higher internal C−O content in CAC-120 compared to the surface C−O content in CAC, likely due to the introduction of additional C−O bonds by pentaborate treatment[33]. In addition, the high-resolution O 1s spectra of CAC-120 can be deconvoluted into 4 components: C=O at 531.6 eV, C−O at 530.2 eV, N−O at 535.2 eV and −COOH at 538.7 eV. Compared with CAC, the C 1s and O 1s core-level spectra of CAC-120 exhibit a shift toward lower binding energies (Fig. 3a and 3b). This reduction in binding energy can be attributed to an increased electron density in the carbon skeleton, resulting from reduced oxygen content and a higher degree of graphitization.

As shown in Fig. 3c, the N 1s signals of CAC-

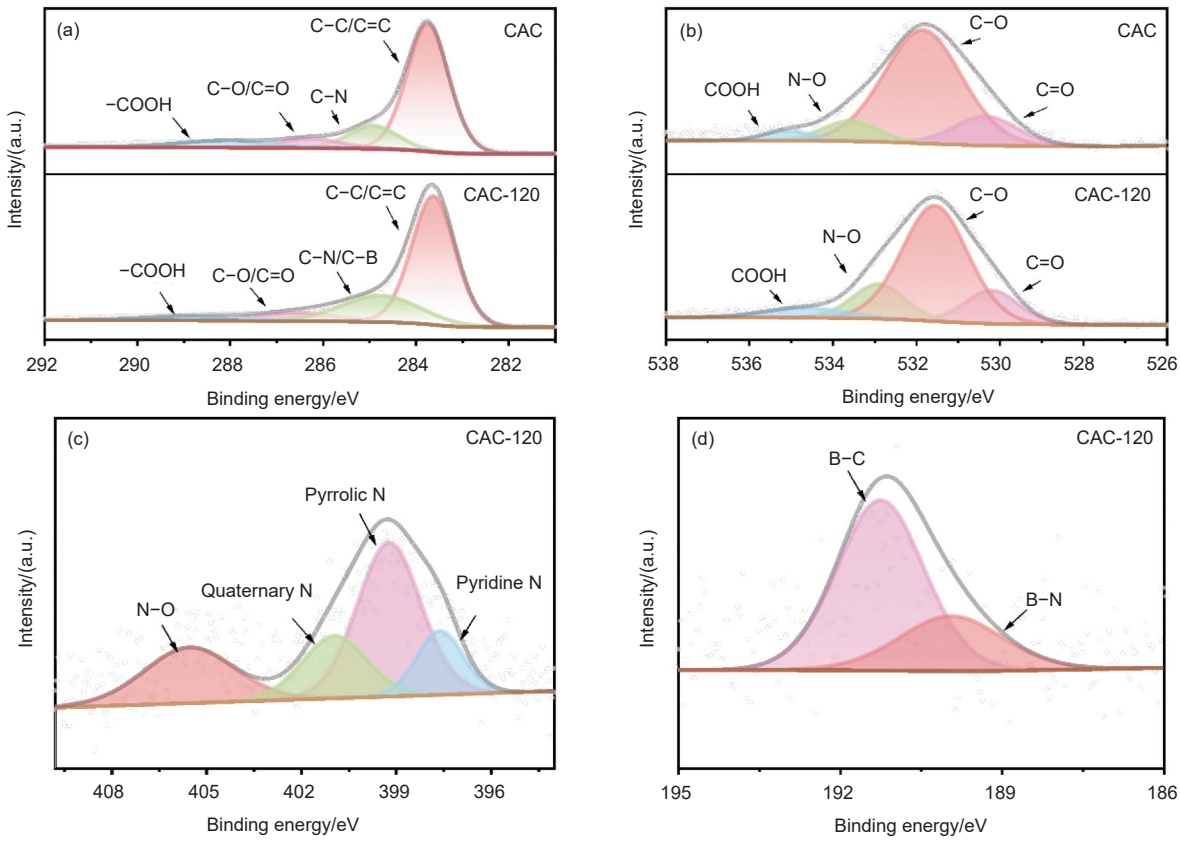

Fig. 3 High resolution XPS spectra of CAC and CAC-120: (a) C 1 s, (b) O 1 s, (c) N 1 s and (d) B 1 s

120 can be deconvoluted into 4 components: pyrrolic N at 399.22 eV, N—O at 405.3 eV, graphitic N at 400.91 eV and pyridine N at 400.6 eV. N doping can enhance the defects and active centers, where the edge N (pyridine N and pyrrole N) could promote charge accumulation. Edge N is considered to enhance electron transfer and conductivity of carbon[34]. This can be inferred from the reduction of C—N bonds in Fig. 3a. This substitution increases pseudo-capacitive sites for Zn^{2+} storage. The high-resolution B 1s spectra of CAC-120 sample demonstrated 2 peaks of B—C at 191.3 eV and B-N at 189.9 eV, respectively. The introduced B—C bond can demonstrate the doping of B atoms in the carbon framework. It is worth noting that B-C can change the electronic structure of carbon skeleton, resulting in the change of electron density and the increase of conductivity[35]. In the process of hydrothermal reaction, C—O increased from 33.62% to 46.5%, while C—C decreased from 66.69% to 62.85%, which can be proven by the appearance of B—C[36–41].

Overall, CAC-120 sample exhibited a significant potential as efficient cathode for zinc-ion capacitors. We hypothesized that the unique interconnected porous structure and high conductivity should facilitate rapid ion diffusion and efficient mass transport, offering superior performance.

Therefore, the electrochemical performances of the CAC and CAC-120 samples were initially evaluated using a standard three-electrode system to analyze their capacitive behaviors in a 2 mol L^{-1} $ZnSO_4$ aqueous solution. The CV curves of CAC and CAC-120 at a scan rate of 5 mV s^{-1} are presented in Fig. 4a, both exhibiting stable profiles within the potential window of -0.6 to 0.4 V. The quasi-rectangular shape of the CV curves exhibits inconspicuous redox signals, highlighting the contributions from electric double-layer capacitance and additional pseudocapacitive effects associated with B and N functional sites on the carbon structure. Notably, the CAC-120 cathode demonstrated a higher current density, as evidenced by its larger integral area. This can be attributed to its abundant N and B co-doped surface functional groups, high specific surface area, and multistage porous structure. Fig. 4b and Fig. S10 show the CV curves of CAC-120 and CAC samples at a scanning rate of 5 to 200 mV s^{-1}, which do not exhibit significant deformation as scan rates increase, manifesting excellent electrochemical kinetics. It is noteworthy that as the scan rate increases, the higher current accelerates ion reaction kinetics, leading to polarization. This results in a positive shift of the oxidation peak and a negative shift of the reduction peak, along with peak broadening and reduced intensity. The specific capacities were measured by GCD tests (Fig. 4c). The discharge capacity of the CAC-120 cathode was calculated to be 371.4 mAh g^{-1} at a current density of 1 A g^{-1} (Fig. S11), exceeding those of the CAC (313.7 mAh g^{-1}, Fig. S11), CAC-150 (245.8 mAh g^{-1}, Fig. S12), and CAC-180 (357.4 mAh g^{-1}, Fig. S12) cathodes. Notably, the quasi-linear GCD curves with inconspicuous discharge plateaus suggest a combined effect of electrical double-layer capacitance and additional electrochemical responses from N and B functional sites, consistent with the CV results. This result confirms that B and N co-doping enhances electrochemical performance by enabling charge storage through reversible Faradaic reactions at the electrode-electrolyte interface. The rate capabilities of the CAC and CAC-120 cathodes are calculated at different current densities of 1, 2, 5, 10 and 20 A g^{-1}, as shown in Fig. 4d. The CAC-120 cathode showed an excellent discharge capacity of 307.5 mAh g^{-1} at a current density of 1 A g^{-1}. When the current density increases to 20 A g^{-1}, the capacity decreases to 159.8 mAh g^{-1}. Thanks to the short ion diffusion path and fast charge transfer kinetics, when returning to the initial current density of 1 A g^{-1}, the capacity recovered to 278.6 mAh g^{-1}, corresponding to a capacity retention rate of 90.6%, higher than that of CAC (85.7%) and material recently reported carbon materials (Table S4).

Electrochemical behavior can be further clarified by EIS. Fig. 4e shows the Nyquist plot of CAC and CAC-120 cathode after fitting, where the equivalent series resistance (R_s) was 4.1 Ω for CAC and 5.5 Ω for

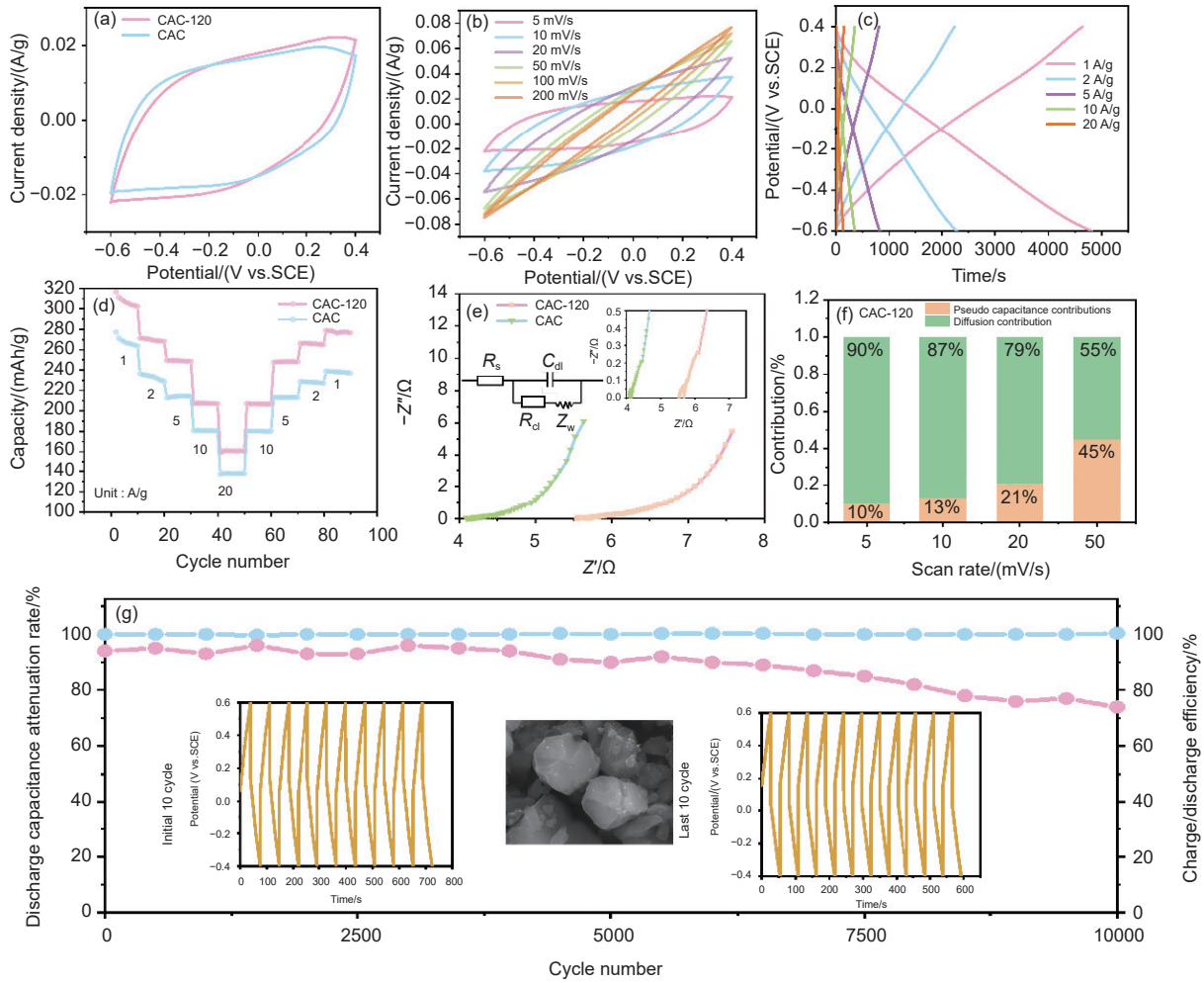

Fig. 4　(a) CV curves of CAC and CAC-120 at a scan rate of 5 mV s^{-1}. (b) CV curves of CAC-120 at different scan rates. (c) GCD curves of CAC-120 at different current densities. (d) Rate performance of CAC and CAC-120. (e) Nyquist plots of CAC-120 and CAC. (f) Capacitance contribution ratio in total capacity of CAC-120. (g) Cycling stability of CAC-120 at 20 A g^{-1}

CAC-120, respectively. In the high frequency region, the compressed semicircle reflects the charge transfer resistance (R_{ct}), while the straight line in the low frequency region is related to the ion diffusion resistance (W) in the electrolyte. CAC-120 cathode shows lower R_{ct} and faster ion diffusion, which can be attributed to the synergistic effect of co-doping of B and N and its porous structure.

The electrochemical kinetics of the electrode can be analyzed by examining the relationship between current and scanning rate. Generally, the relationship between current (i) and scanning rate (v) follows the following Eq. (5)[42]:

$$i = av^b \tag{5}$$

where a and b are adjustable constants. A b value of 0.5 usually indicates that the energy storage process is controlled by diffusion, while a b value of 1.0 indicates the surface capacitance limiting process. For the CAC-120 cathode, the obtained b values were 0.94 for the anodic peak and 0.96 for the cathodic peak. Meanwhile, the b values for the CAC cathode were 0.82 for the anodic peak and 0.85 for the cathodic peak. The ultrafast charge storage kinetics of CAC-120 cathode was confirmed. Meanwhile, the contribution of capacitance-dominated and diffusion-dominated processes can be quantified using the following equation[43]:

$$i = k_1 v + k_2 v^{0.5} \tag{6}$$

where k_1 and k_2 represent the ratios of pseudocapacitive and diffusive contributions, respectively.

As shown in Fig. S14, the surface-controlled contribution of the CAC cathode increased from 19% at 5 mV s^{-1} to 57% at 50 mV s^{-1}, while the diffusion-

controlled contribution diminished as the scan rate increased, indicating that the surface reaction plays a significant role. Meanwhile (Fig. 4f), the surface control contribution of the CAC-120 cathode increased from 10% at 5 mV s^{-1} to 45% at 50 mV s^{-1}, indicating that Faradaic reactions involving surface heteroatoms make a significant contribution to the charge storage mechanism in the CAC-120 cathode. Fig. 4g and Fig. S15 illustrate the cycling performance of the CAC-120 and CAC cathodes at a current density of 20 A g^{-1}. The CAC-120 cathode maintained an impressive capacity retention rate of 74% after 10 000 cycles, higher than that of ~ 50% after 7000 cycles CAC cathode, demonstrating excellent cyclic stability. The inset in Fig. 4g shows the GCD curves for the first 10 and last 10 cycles of the CAC-120 cathode, revealing no significant changes over the charge/discharge testing period. The SEM image after cycling further confirmed the structural stability of CAC-120 cathode due to basically unchanged morphology. Moreover, the coulombic efficiency of the CAC-120 cathode was consistently maintained at approximately 100%, indicating superior electrochemical reversibility.

To achieve a more comprehensive understanding of the charge storage mechanism in CAC-120 cathode, ex-situ XPS and Raman analyses were conducted at different charge and discharge states during the electrochemical process. The electrodes at 7 key points along the GCD curve have been illustrated in Fig. 5a. These points are labeled A, B, C and D, corresponding to −0.6, −0.25, 0.1 and 0.4 V during the charge process, respectively. Additionally, points E, F and G represent 0.1, −0.25 and −0.6 V during the discharge process. To gain deeper insights into the energy storage behavior, ex-situ Raman spectroscopy was utilized (Fig. 5b). The *D* and *G* band features showed minimal variations throughout the charging and discharging cycles, indicating that the charge storage mechanism is predominantly driven by chemical adsorption and desorption processes. To investigate the electrochemical adsorption of Zn^{2+} on the C, O, N and B of CAC-120 cathode, ex-situ XPS spectra of the cathode were examined (Fig. 5c-5d and Fig. S16-S17). Fig. 5c shows the deconvoluted C 1s spectra, which provides insight into the possible chemical transformation between doped atoms and Zn^{2+}. A new characteristic peak appears at 287.3 eV, which belongs to C—O—Zn bond. The intensity of this C—O—Zn peak increases with the progression of charging and gradually decreases during the discharging process, indicating the excellent reversibility of chemisorption between doping atoms and Zn^{2+}[44].

During charging, the C—O—Zn/C—O area ratio increases from 3.33% to 89.3%, then decreases from 89.3% to 1.22% upon discharging (Fig. 5d). This reversible change, mirrored by the decreasing C—O peak intensity during charge and its increase during discharge in the O 1s spectra, demonstrates that C—O bonds actively participate in electrochemical redox reactions by the formation of C—O—Zn complexes[45–47]. Fig. 5d shows the deconvoluted O 1s spectra. The peak intensity of the C-O bond gradually decreases during charging and increases during the discharge process, demonstrating that the C—O bond actively participates in the electrochemical redox reaction through the formation of a carbon-oxygen-zinc complex. These observations indicate that the formation of C—O—Zn bonds is reversible processes during charge and discharge cycles. Fig. S16 and S17 present the deconvoluted B 1s and N 1s spectra, respectively, which provide insights into the potential reactions between heteroatoms and Zn ions by examining the details of chemical transformations. As illustrated in Fig. S16, the intensity of the B—N peak progressively diminishes during the charging process, whereas it steadily increases throughout the discharging process. As to N 1s peak, the peak intensity of Pyrrolic N area decreases from 49.95% to 32.56% during charging and increases from 32.56% to 40.64% upon discharging, which indicated a zincation reaction during the charge process and an extrusion of Zn^{2+} during the discharging process.

In order to grasp the influence of N doping for the adsorption performance of CAC-120, a cluster model was used to perform DFT calculations on vari-

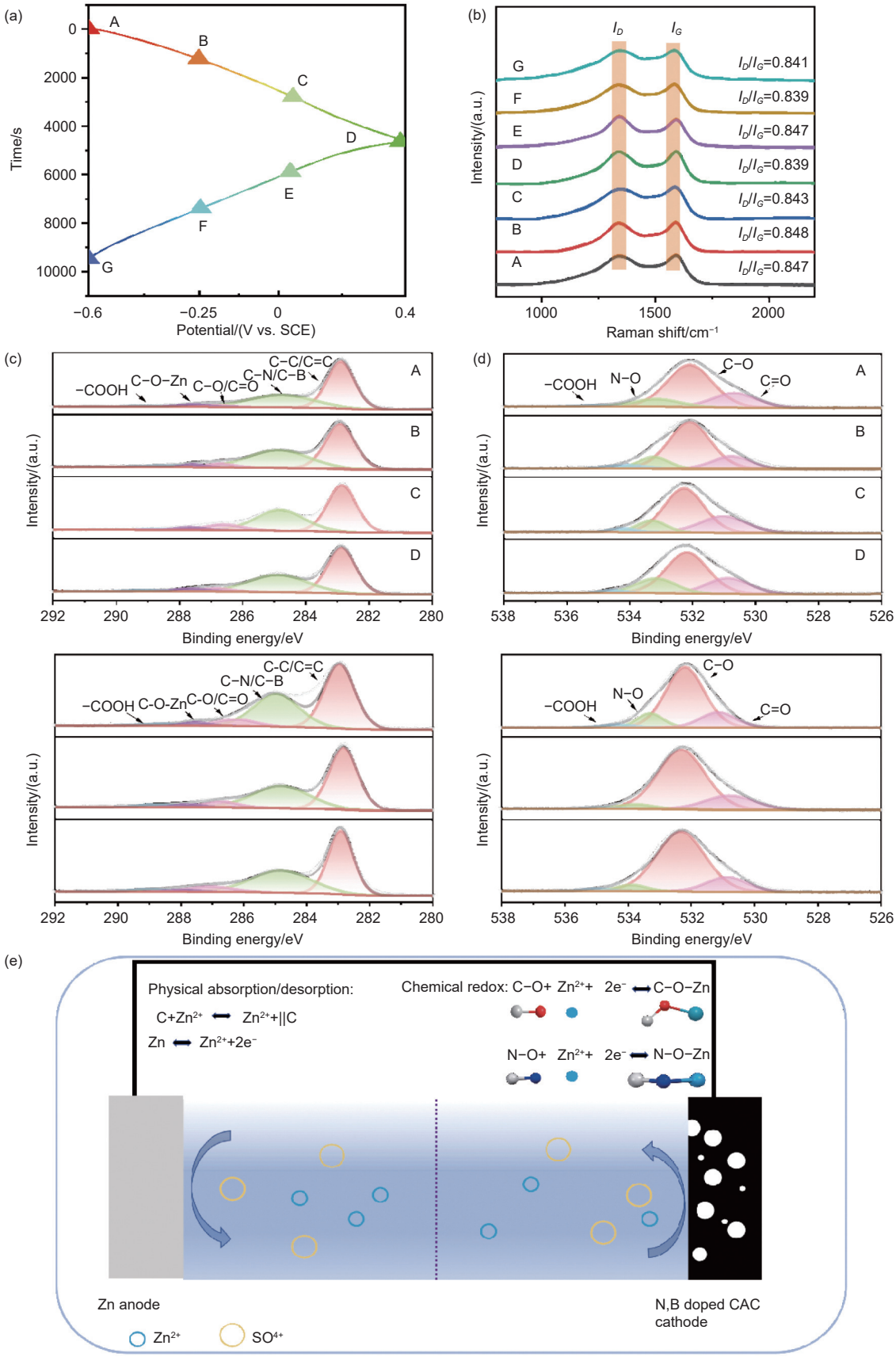

Fig. 5 Study on reaction mechanism of CAC-120 cathode electrode: (a) GCD curves at 1 A g^{-1} and 7 points ing different charge and discharge states. (b) Ex-situ Raman. High-resolution XPS of CAC-120 cathodes obtained during discharging–charging processes: (c) C 1s and (d) O 1s. (e) Schematic illustration of the preparation process of CAC-120

ous carbon surfaces containing pyrrolic N, pyridinic N, graphitic N and B[46]. This helped explain the energy storage mechanism of CAC-120 during the Zn ion adsorption/desorption process comprehensively.

As shown in Fig. 6, the adsorption energy (E_a) value for Zn ions on the pyrrolic N site and pyridinic N site is −0.1 and −0.12 eV, respectively, which are higher than that on graphitic N (−0.2 eV) and B (−0.25 eV). Compared with B and graphitic N, pyrrolic N and pyridinic N doping can directly bind to Zn^{2+} with a higher E_a, thereby providing more adsorption sites for electrolyte ion adsorption. This verifies that edge nitrogen can enhance the adsorption ability of Zn ions. The theoretical findings indicate that the heteroatom not only facilitate the kinetics of Zn ion adsorption but also improve the pseudocapacitive performance of CAC-120 cathode.

A ZIC was assembled used CAC-120 as cathode and a Zn plate as anode to further verify the practicability of the CAC-120 sample. The CV curves at different scan rates are shown in Fig. 7a. The ZIC could be operated stably over a voltage range of 0 to 2 V. The

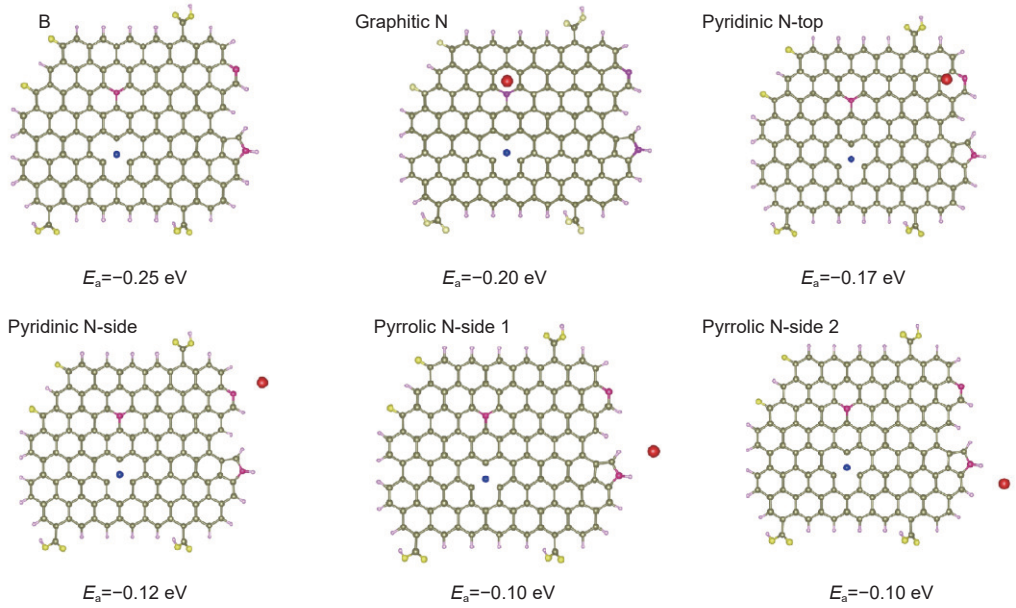

Fig. 6 Density functional calculation of zinc ion adsorption energy on CAC-120

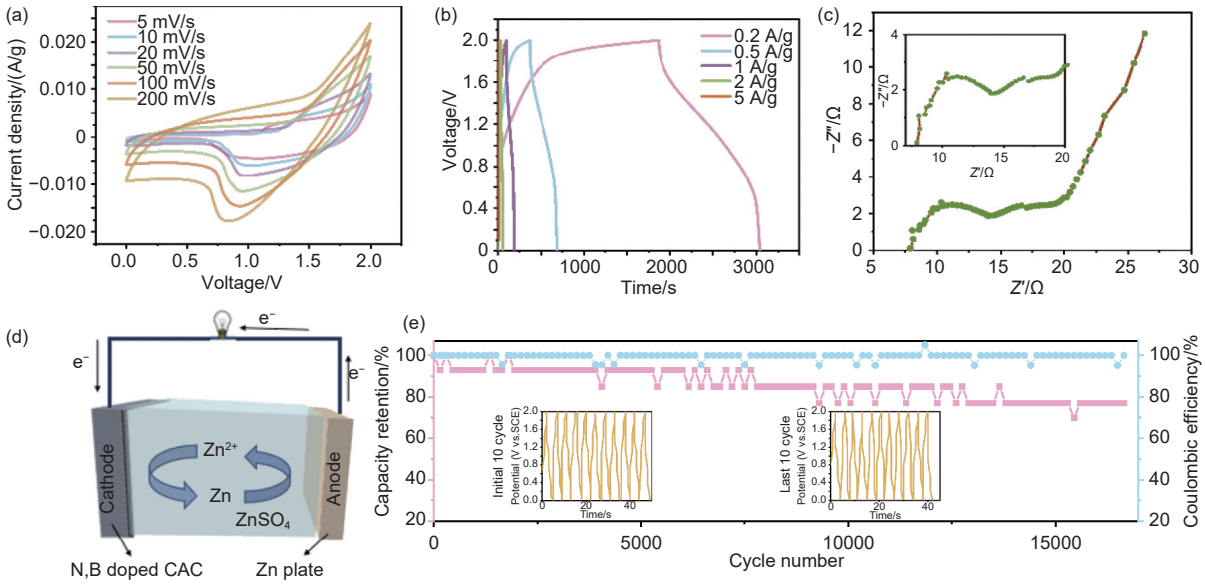

Fig. 7 (a) ZIC at different scan rates. (b) GCD curves at different scan rates. (c) Nyquist plots. (d) Schematic diagram. (e) Cycling stability of CAC-120 at 1 A g^{-1}

GCD curves were obtained from 0.2 to 5 A g^{-1} (Fig. 7b). The ZIC delivered a specific capacity of 90.8 mAh g^{-1} at 0.2 A g^{-1}. The Nyquist plots of the ZIC are shown in Fig. 7c, exhibiting a low R_{ct} value of 7.5 Ω, which reflects the rapid transport of Zn^{2+} in the ZIC. The cycling performance of ZIC is illustrated in Fig.7e. The ZIC exhibited an impressive durability of 17 000 charge-discharge cycles, with a capacitance retention of 77% and a coulombic efficiency of nearly 100%. The above test results demonstrate the great potential of ZIC as an energy storage device for electronic applications.

4 Conclusion

In summary, CAC-120, engineered with an optimal pore size distribution and N/B heteroatom doping, serves as a high-performance cathode for Zn-ion storage. Its high surface area, tailored porosity, and heteroatom doping act synergistically to provide abundant accessible active sites and enhanced kinetics for Zn^{2+} insertion. Consequently, CAC-120 delivers outstanding electrochemical performance: a high specific capacity of 371.4 mAh g^{-1}, excellent reversibility (90.6% capacity retention), and remarkable cycling stability (74% capacity retention after 10 000 cycles). Electrochemical analysis and DFT calculations confirm the critical role of edge-N sites in facilitating Zn^{2+} transport kinetics. Furthermore, an assembled aqueous ZIC using the CAC-120 cathode achieves a high reversible capacity of 90.8 mAh g^{-1} at 0.2 A g^{-1} and exceptional long-term stability over 17 000 cycles. This work presents a facile strategy for designing high-performance carbon cathodes via precise pore structure engineering and heteroatom doping for advanced aqueous zinc-based energy storage systems.

Copyright contribution statement

Liu Shuyuan: Investigation, Writing-original draft. Tian Zhen: Formal analysis, Writing-review & editing, Funding acquisition. Wang Yanzhong: Formal analysis, Conceptualization. Zhou Rui: Conceptualization. Chen Yanjun: Conceptualization. Zheng Zhichao: Conceptualization.

Acknowledgements

This work was supported by National Natural Science Foundation of China (52202051), the Key Research and Development (R&D) Projects of Shanxi Province (202202040201005). The authors extend their gratitude to Zhang Huifang (from Scientific Compass www.shiyanjia.com) for providing invaluable assistance with the measurement analysis.

References

[1] Zhao H Y, Wang L X, Jia D Z, et al. Coal based activated carbon nanofibers prepared by electrospinning[J]. Journal of Materials Chemistry A, 2014, 2(24): 9338-9344.

[2] Li C, An Y B, Wang L, et al. Balancing microcrystalline domains in hard carbon with robust kinetics for a 46.7 Wh kg^{-1} practical lithium-ion capacitor[J]. Chemical Engineering Journal, 2024, 485: 149880.

[3] Song S, Zhang X, An Y B, et al. Lifetime prediction of lithium-ion capacitors using electro-thermal-aging co-simulation platform[J]. Journal of Energy Storage, 2024, 85: 111088.

[4] Du T, Liu Z E, Sun X Z, et al. Segmented bi-material cathodes to boost the lithium-ion battery-capacitors[J]. Journal of Power Sources, 2020, 478: 228994.

[5] Qiu C, Zhu X H, Xue L, et al. The function of Mn^{2+} additive in aqueous electrolyte for Zn/δ-MnO_2 battery[J]. Electrochimica Acta, 2020, 351: 136445.

[6] Song M, Tan H, Chao D L, et al. Recent advances in Zn-ion batteries[J]. Advanced Functional Materials, 2018, 28(41): 1802564.

[7] Wu X Y, Markir A, Xu Y K, et al. A rechargeable battery with an iron metal anode[J]. Advanced Functional Materials, 2019, 29(20): 1900911.

[8] Zeng X H, Hao J N, Wang Z J, et al. Recent progress and perspectives on aqueous Zn-based rechargeable batteries with mild aqueous electrolytes[J]. Energy Storage Materials, 2019, 20: 410-437.

[9] Liu Z X, Luo X B, Qin L P, et al. Progress and prospect of low-temperature zinc metal batteries[J]. Advanced Powder Materials, 2022, 1(2): 100011.

[10] Ge L C, Zhao C, Chen S M, et al. An analysis of the carbonization process and volatile-release characteristics of coal-based activated carbon[J]. Energy, 2022, 257: 124779.

[11] Liu Q S, Zheng T, Wang P, et al. Preparation and characterization of activated carbon from bamboo by microwave-induced phosphoric acid activation[J]. Industrial Crops and Products, 2010, 31(2): 233-238.

[12] Heidarinejad Z, Dehghani M H, Heidari M, et al. Methods for preparation and activation of activated carbon[J]. Environmental Chemistry Letters, 2020, 18(2): 393-415.

[13] Kundu D, Adams B D, Duffort V, et al. A high-capacity and long-life aqueous rechargeable zinc battery using a metal oxide intercalation cathode[J]. Nature Energy, 2016, 1(10): 1-8.

[14] Kumar R, Sahoo S, Joanni E, et al. Heteroatom doped graphene engineering for energy storage and conversion[J]. Materials Today, 2020, 39: 47-65.

[15] Miao L, Duan H, Zhu D Z, et al. Boron "gluing" nitrogen heteroatoms in a prepolymerized ionic liquid-based carbon scaffold for durable supercapacitive activity[J]. Journal of Materials Chemistry A, 2021, 9(5): 2714-2724.

[16] Zhao J, Li Y J, Wang G L, et al. Enabling high-volumetric-energy-density supercapacitors: designing open, low-tortuosity heteroatom-doped porous carbon-tube bundle electrodes[J]. Journal of Materials Chemistry A, 2017, 5(44): 23085-23093.

[17] Chang X Q, Ma Y F, Yang M, et al. In-situ solid-state growth of N, S codoped carbon nanotubes encapsulating metal sulfides for high-efficient-stable sodium ion storage[J]. Energy Storage Materials, 2019, 23: 358-366.

[18] Lu Z W, Xu X C, Chen Y J, et al. Nitrogen and sulfur co-doped graphene aerogel with hierarchically porous structure for high-performance supercapacitors[J]. Green Energy Environment, 2020, 5(1): 69-75.

[19] Fan L L, Shi Z Q, Ren Q J, et al. Nitrogen-doped lignin based carbon microspheres as anode material for high performance sodium ion batteries[J]. Green Energy Environment, 2021, 6(2): 220-228.

[20] Béguin F, Presser V, Balducci A, et al. Carbons and electrolytes for advanced supercapacitors[J]. Advanced materials, 2014, 26(14): 2219-2251.

[21] Yin J, Zhang W L, Wang W X, et al. Electrochemical zinc ion capacitors enhanced by redox reactions of porous carbon cathodes[J]. Advanced Energy Materials, 2020, 10(37): 2001705.

[22] Song T B, Ma Q L, Wang B J, et al. High-capacity and long-life cathode constructed solely by carbon dots for aqueous zinc-ion batteries[J]. Angewandte Chemie International Edition, 2025, 64(34): e202503655.

[23] Jiang X G, Kyriakou V, Song C, et al. A novel multi-channel porous structure facilitating mass transport towards highly efficient alkaline water electrolysis[J]. Journal of Energy Chemistry, 2024, 93: 511-518.

[24] Lu J, Wang C L, Yu H L, et al. Oxygen fluorine dual-doped porous carbon nanopolyhedra enabled ultrafast and highly stable potassium storage[J]. Advanced Functional Materials, 2019, 29(49): 1906126.

[25] Ferrari A C, Robertson J. Interpretation of Raman spectra of disordered and amorphous carbon[J]. Physical Review, 2000, 61(20): 14095.

[26] Dresselhaus M S, Jorio A, Hofmann M, et al. Perspectives on carbon nanotubes and graphene Raman spectroscopy[J]. Nano letters, 2010, 10(3): 751-758.

[27] Gupta H, Rathore H K, Kumar M, et al. Bitter apple pulp-derived porous carbon with rich oxygen functionalities for high-performance zinc-ion storage[J]. Small, 2025, 21(30): 2502071.

[28] Sadezky A, Muckenhuber H, Grothe H, et al. Raman microspectroscopy of soot and related carbonaceous materials: Spectral analysis and structural information[J]. Carbon, 2005, 43(8): 1731-1742.

[29] Xia J S, Zhang N, Chong S K, et al. Three-dimensional porous graphene-like sheets synthesized from biocarbon via low-temperature graphitization for supercapacitor[J]. Green Chemistry, 2018, 20(3): 694-700.

[30] Sing K. The use of nitrogen adsorption for the characterisation of porous materials[J]. Colloids and Surfaces A, 2001, 187: 3-9.

[31] Ma X P, Cheng J Y, Dong L B, et al. Multivalent ion storage towards high-performance aqueous zinc-ion hybrid supercapacitors[J]. Energy Storage Materials, 2019, 20: 335-342.

[32] Li H X, Wu J, Wang L T, et al. A zinc ion hybrid capacitor based on sharpened pencil-like hierarchically porous carbon derived from metal-organic framework[J]. Chemical Engineering Journal, 2022, 428: 131071.

[33] Zhao C Y, Lin Y M, Lin Q Y, et al. C—P/C=O bonds assisted desolvation effect in ultra-micropores carbon for boosting Zn-ion storage capability[J]. Energy Storage Materials, 2023, 58: 332-343.

[34] Shi X, Zhang H Z, Zeng S Q, et al. Pyrrolic-dominated nitrogen redox enhances reaction kinetics of pitch-derived carbon materials in aqueous zinc ion hybrid supercapacitors[J]. ACS Materials Letters, 2021, 3(9): 1291-1299.

[35] Wang L, Wang Y Q, Wu M G, et al. Nitrogen, fluorine, and boron ternary doped carbon fibers as cathode electrocatalysts for zinc-air batteries[J]. Small, 2018, 14(20): 1800737.

[36] Sun F, Qu Z B, Gao J H, et al. In-situ doping boron atoms into porous carbon nanoparticles with increased oxygen graft enhances both affinity and durability toward electrolyte for greatly improved supercapacitive performance[J]. Advanced Functional Materials, 2018, 28(41): 1804190.

[37] Wang D W, Li F, Chen Z G, et al. Synthesis and electrochemical property of boron-doped mesoporous carbon in supercapacitor[J]. Chemistry of Materials, 2008, 20(22): 7195-7200.

[38] Radovic L R, Karra M, Skokova K, et al. The role of substitutional boron in carbon oxidation[J]. Carbon, 1998, 36(12): 1841-1854.

[39] Liu K L, Yu C, Guo W, et al. Recent research advances of self-discharge in supercapacitors: mechanisms and suppressing strategies[J]. Energy Chemistry Journal, 2021, 58: 94-109.

[40] Yang X, Zhao, X H, et al. Highly active and selective oxygen reduction to H_2O_2 on boron-doped carbon for high production rates[J]. Nature Communicatioons, 2021(12): 4225.

[41] Fan W J, Ding J, Ding J N, et al. Identifying heteroatomic and defective sites in carbon with dual-ion adsorption capability for high energy and power zinc ion capacitor[J]. Nano-Micro Letters, 2021, 13(1): 59.

[42] Liu Y, Zhao S Q, Wu X, et al. High-performance VS_2-based aqueous zinc ion batteries by the co-intercalation of Zn^{2+}/Na^{+}[J]. Crystal Growth & Design, 2025.

[43] Shi J J, Hou Y X, Liu Z Y, et al. The high-performance MoO_{3-x}/MXene cathodes for zinc-ion batteries based on oxygen vacancies and electrolyte engineering[J]. Nano Energy, 2022, 91: 106651.

[44] Zhang H Z, Liu Q Y , Fang Y B, et al. Boosting Zn-ion energy storage capability of hierarchically porous carbon by promoting chemical adsorption[J]. Advanced Materials, 2019, 31(44): 1904948.

[45] Sun G Q, Yang H S, Zhang G F, et al. A capacity recoverable zinc-ion micro-supercapacitor[J]. Energy & Environmental Science, 2018, 11(12): 3367-3374.

[46] Cui J, Guo Z W, Yi J, et al. Organic cathode materials for rechargeable zinc batteries: mechanisms, challenges, and perspectives[J]. ChemSusChem, 2020, 13(9): 2160-2185.

[47] Zheng Y, Jiao Y, Jaroniec M, et al. Two-step boron and nitrogen doping in graphene for enhanced synergistic catalysis[J]. Angewandte Chemie International Edition, 2013, 52: 3110-3116.